

This is the accepted manuscript made available via CHORUS. The article has been published as:

Thermoelectric and thermal transport in bilayer graphene systems

R. Ma, L. Zhu, L. Sheng, M. Liu, and D. N. Sheng

Phys. Rev. B **84**, 075420 — Published 5 August 2011

DOI: [10.1103/PhysRevB.84.075420](https://doi.org/10.1103/PhysRevB.84.075420)

Thermoelectric and thermal transport in bilayer graphene systems

R. Ma,^{1,2} L. Zhu,³ L. Sheng,⁴ M. Liu,⁵ and D.N Sheng²

¹*Faculty of Mathematics and Physics, Nanjing University of Information Science and Technology, Nanjing 210044, China*

²*Department of Physics and Astronomy, California State University, Northridge, California 91330, USA*

³*Theoretical Division and Center for Nonlinear Studies,*

Los Alamos National Laboratory, Los Alamos, NM 87545, USA

⁴*National Laboratory of Solid State Microstructures and Department of Physics, Nanjing University, Nanjing 210093, China*

⁵*Department of Physics, Southeast University, Nanjing 210096, China*

We numerically study the disorder effect on the thermoelectric and thermal transport in bilayer graphene under a strong perpendicular magnetic field. In the unbiased case, we find that the thermoelectric transport has similar properties as in monolayer graphene, i.e., the Nernst signal has a peak at the central Landau level (LL) with a height of the order of k_B/e and changes sign near other LLs, while the thermopower has an opposite behavior. We attribute this to the coexistence of particle and hole LLs around the Dirac point. When a finite interlayer bias is applied and a band gap is opened, it is found that the transport properties are consistent with those of a band insulator. We further study the thermal transport from electronic origin and verify the validity of the generalized Weidemann-Franz law.

PACS numbers: 72.80.Vp; 72.10.-d; 73.50.Lw, 73.43.Cd

I. INTRODUCTION

Thermoelectric transport properties of graphene have recently attracted much experimental¹⁻³ and theoretical⁴⁻⁹ attention. The thermopower (the longitudinal thermoelectric response) and the Nernst signal (the transverse response) in the presence of a strong magnetic field are found to be large, reaching the order of the quantum limit k_B/e , where k_B and e are the Boltzmann constant and the electron charge, respectively¹⁻³. This has been attributed to the semi-metal type dispersion of graphene and/or in the vicinity of a quantum Hall liquid to insulator transition where the imbalance between the particle and hole types of carriers is significant. The thermoelectric effects are very sensitive to such an imbalance and become large in comparison with conventional metals.

In our previous study on graphene in the presence of disorder and an external magnetic field⁹, we have shown that its thermoelectric transport properties are determined by the interplay of the unique band structure, the disorder-induced scattering, the Landau quantization and the temperature. While the band structure and the magnetic field determine the Landau level (LL) spectrum, the broadening of each LL is controlled by the competition between disorder-induced scattering and the thermal activation. We find that all transport coefficients are universal functions of W_L/E_F and k_BT/E_F when both W_L and k_BT are much smaller than the Landau quantization energy $\hbar\omega_c$. Here, W_L is the width of the central LL (W_L is determined by the full width at half-maximum of the longitudinal conductivity σ_{xx} peak). E_F and T are the Fermi energy and the temperature, respectively. When $k_BT \ll W_L$, the thermoelectric conductivities vary as the density of states (and the particle-hole symmetry) is tuned by E_F from the center of the LL to the mobility gap. When $k_BT \gg W_L$, thermal activation

dominates and certain peak values of the thermopower S_{xx} or the Nernst signal S_{xy} reach universal numbers independent of the magnetic field or the temperature. While both S_{xx} and S_{xy} near high LLs ($\nu \neq 0$) have similar behaviors to those in two-dimensional (2D) semiconductor systems displaying the integer quantum Hall effect (IQHE)¹⁰⁻¹³, they have opposite behaviors around the central LL. S_{xy} has a peak while S_{xx} vanishes and changes sign at the Dirac point ($E_F = 0$). We have further argued that the unique behavior at the central LL is due to the coexistence of particle and hole LLs. As protected by the particle-hole symmetry, the contributions from particle and hole LLs cancel with each other exactly in the thermopower but superpose in the Nernst signal. The results for such a tight-binding analysis are in good agreement with the experimental observations¹⁻³.

In this work, we extend our study to bilayer graphene which has two parallel graphene sheets stacked on top of each other as in 3D graphite (the AB or Bernal stacking). While some common features are observed related to LLs with the same underlying particle-hole symmetry, bilayer graphene also demonstrates some interesting and different properties from monolayer graphene¹⁴⁻¹⁹. The low energy dispersion of bilayer graphene can be effectively given by two hyperbolic bands $\epsilon_k \approx \pm k^2/(2m^*)$ touching each other at the Dirac point ($E_F = 0$), i.e., the electrons or holes have a finite mass m^* which is in contrast to the massless excitations in monolayer graphene. Another important difference of bilayer graphene is the possibility to open up a band gap with a bias voltage, or a potential difference, applied between the two layers. This tunable gap system is advantageous to conventional semiconductor materials, making bilayer graphene more appealing from the point of view of applications. The thermoelectric transport properties of bilayer graphene are also expected to be interesting. The thermopower of bilayer graphene without a magnetic field has been con-

sidered²⁰. It is shown that as the density of states is also of the pseudogap type without a biased voltage, one expects that the relation for the thermopower $S_{xx} \sim T/E_F$ continues to hold. In addition, it is found that the room-temperature thermopower with a bias voltage can be enhanced by a factor of 4 than that of the value in monolayer graphene or unbiased bilayer graphene²⁰, making it a more promising candidate for future thermoelectric applications. Our study is to consider the thermopower and the Nernst effect under a magnetic field.

When an external magnetic field B is applied, as in graphene and other IQHE systems, electron energies of bilayer graphene are quantized into Landau levels. As the band dispersion changes, these LLs follow a different quantization sequence $E_n = \pm \sqrt{n(n-1)}\hbar\omega_c$ with $\omega_c \sim B$ from \sqrt{B} for graphene. This has been confirmed by the theoretical²¹ and experimental²² studies on the quantum Hall effects, and further verified by our numerical calculation²³. Compared with graphene, though the massive nature of particles and hyperbolic dispersion are different, the existence of the central LL ($\nu = 0$) and the associated chiral and particle-hole symmetries are preserved. Therefore, the study on the thermoelectric transport in bilayer graphene not only provides theoretical predictions for their properties, in particular, their dependence on disorder and magnetic field for this system, but also helps to verify our argument on the central LL that its unique behavior is due to the chiral and particle-hole symmetries associated with the Dirac point.

For such purposes, we carry out a numerical study of the thermoelectric transport in both unbiased and biased bilayer graphene. We focus on studying the effects of disorder and thermal activation on the broadening of LLs and the corresponding thermoelectric transport properties. In the unbiased case, we indeed observe similar behaviors as in monolayer graphene for the central LL. Both the longitudinal and the transverse thermoelectric conductivities are universal functions of W_L/E_F and $k_B T/E_F$ and display different asymptotic behaviors in different temperature regions. The calculated Nernst signal has a peak at the central LL with a height of the order of k_B/e , and changes sign near other LLs, while the thermopower has an opposite behavior. A higher peak value is obtained comparing to graphene due to the doubled degeneracy. This confirms our argument that as the particle and hole LLs coexist only in the central LL, the thermopower vanishes while the Nernst effect has a peak structure. As before, we verify the validity of the semi-classical Mott relation, which is shown to hold in a wide range of temperatures. When a bias is applied between the two graphene layers, the thermoelectric coefficients exhibit unique characteristics quite different from those of unbiased case. Around the Dirac point, the transverse thermoelectric conductivity exhibits a pronounced valley with $\alpha_{xy} = 0$ at low temperatures, and the thermopower displays a very large peak. We show that these features are associated with a band insulator, due to the opening of a sizable gap between the valence and con-

duction bands in biased bilayer graphene. In addition, we have calculated the thermal transport properties of electrons for both unbiased and biased bilayer graphene systems. In the biased case, it is found that the transverse thermal conductivity displays a pronounced plateau with $\kappa_{xy} = 0$, which is accompanied by a valley in κ_{xx} . This provides additional evidence for the band insulator behaviors. We further compare the calculated thermal conductivities with those deduced from the Wiedemann-Franz law, to check the validity of this fundamental relation in graphene systems.

This paper is organized as follows. In Sec. II, we introduce the model Hamiltonian. In Sec. III and Sec. IV, numerical results based on exact diagonalization and thermoelectric transport calculations are presented for unbiased and biased systems, respectively. In Sec. V, numerical results for thermal transport are presented. The final section contains a summary.

II. MODEL AND METHODS

We consider a bilayer graphene sample consisting of two coupled hexagonal lattices including inequivalent sublattices A, B on the bottom layer and \tilde{A}, \tilde{B} on the top layer. The two layers are arranged in the AB (Bernal) stacking^{24,25}, where B atoms are located directly below \tilde{A} atoms, and A atoms are the centers of the hexagons in the other layer. Here, the in-plane nearest-neighbor hopping integral between A and B atoms or between \tilde{A} and \tilde{B} atoms is denoted by $\gamma_{AB} = \gamma_{\tilde{A}\tilde{B}} = \gamma_0$. For the interlayer coupling, we take into account the largest hopping integral between B atom and the nearest \tilde{A} atom $\gamma_{\tilde{A}B} = \gamma_1$, and the smaller hopping integral between an A atom and three nearest \tilde{B} atoms $\gamma_{A\tilde{B}} = \gamma_3$. The values of these hopping integrals are taken to be $\gamma_0 = 3.16$ eV, $\gamma_1 = 0.39$ eV, and $\gamma_3 = 0.315$ eV, as same as in Ref.²³.

We assume that each monolayer graphene has totally L_y zigzag chains with L_x atomic sites on each chain²⁶. The size of the sample will be denoted as $N = L_x \times L_y \times L_z$, where $L_z = 2$ is the number of monolayer graphene planes along the z direction. We have confirmed that the calculated results does not depend on the system sizes (as long as the system lengths are reasonably large, not much smaller than 24)²³. We model charged impurities in substrate, randomly located in a plane at a distance d from the graphene sheet with long-range Coulomb scattering potentials²⁷⁻³⁰. This type of disorder is known to give more satisfactory results for transport properties of graphene in the absence of a magnetic field³¹. When a magnetic field is applied perpendicular to the bilayer graphene plane, the Hamiltonian can be written in the tight-binding form

$$\begin{aligned}
H_0 = & -\gamma_0 \left(\sum_{\langle ij \rangle \sigma} e^{ia_{ij}} c_{i\sigma}^\dagger c_{j\sigma} + \sum_{\langle ij \rangle \sigma} e^{ia_{ij}} \tilde{c}_{i\sigma}^\dagger \tilde{c}_{j\sigma} \right) \\
& - \gamma_1 \sum_{\langle ij \rangle_{1\sigma}} e^{ia_{ij}} c_{j\sigma B}^\dagger \tilde{c}_{i\sigma \tilde{A}} - \gamma_3 \sum_{\langle ij \rangle_{3\sigma}} e^{ia_{ij}} c_{i\sigma A}^\dagger \tilde{c}_{j\sigma \tilde{B}} + h.c. \\
& + \sum_{i\sigma} w_i (c_{i\sigma}^\dagger c_{i\sigma} + \tilde{c}_{i\sigma}^\dagger \tilde{c}_{i\sigma}), \tag{1}
\end{aligned}$$

where $c_{i\sigma}^\dagger$ ($c_{i\sigma A}^\dagger$), $c_{j\sigma}^\dagger$ ($c_{j\sigma B}^\dagger$) are creation operators on A and B sublattices in the bottom layer, and $\tilde{c}_{i\sigma}^\dagger$ ($\tilde{c}_{i\sigma \tilde{A}}^\dagger$), $\tilde{c}_{j\sigma}^\dagger$ ($\tilde{c}_{j\sigma \tilde{B}}^\dagger$) are creation operators on \tilde{A} and \tilde{B} sublattices in the top layer, with σ as a spin index. The sum $\sum_{\langle ij \rangle \sigma}$ denotes the intralayer nearest-neighbor hopping in both layers, $\sum_{\langle ij \rangle_{1\sigma}}$ stands for interlayer hopping between the B sublattice in the bottom layer and the \tilde{A} sublattice in the top layer, and $\sum_{\langle ij \rangle_{3\sigma}}$ stands for the interlayer hopping between the A sublattice in the bottom layer and the \tilde{B} sublattice in the top layer, as described above. The magnetic flux per hexagon $\phi = \sum_{\square} a_{ij} = \frac{2\pi}{M}$ is proportional to the strength of the applied magnetic field B , where M is assumed to be an integer and the lattice constant is taken to be unity. For charged impurities, $w_i = -\frac{Ze^2}{\epsilon} \sum_{\alpha} 1/\sqrt{(\mathbf{r}_i - \mathbf{R}_{\alpha})^2 + d^2}$, where Ze is the charge carried by an impurity, ϵ is the effective background lattice dielectric constant, and \mathbf{r}_i and \mathbf{R}_{α} are the planar positions of site i and impurity α , respectively. All the properties of the substrate (or vacuum in the case of suspended graphene) can be absorbed into a dimensionless parameter $r_s = Ze^2/(\epsilon \hbar v_F)$, where v_F is the Fermi velocity of the electrons. For simplicity, in the following calculation, we fix the distance $d = 1\text{nm}$ and impurity density as 1% of the total sites, and tune r_s to control the impurity scattering strength. The characteristic features of the calculated transport coefficients are insensitive to choice of these parameters.

For the biased system, the two graphene layers gain different electrostatic potentials, and the corresponding energy difference is given by $\Delta_g = \epsilon_2 - \epsilon_1$ where $\epsilon_1 = -\frac{1}{2}\Delta_g$, and $\epsilon_2 = \frac{1}{2}\Delta_g$. The Hamiltonian can be written as: $H = H_0 + \sum_{i\sigma} (\epsilon_1 c_{i\sigma}^\dagger c_{i\sigma} + \epsilon_2 \tilde{c}_{i\sigma}^\dagger \tilde{c}_{i\sigma})$. For illustrative purpose, a relatively large asymmetric gap $\Delta_g = 0.1\gamma_0$ is assumed, which is however experimentally achievable¹⁸.

In the linear response regime, the charge current in response to an electric field or a temperature gradient can be written as $\mathbf{J} = \hat{\sigma} \mathbf{E} + \hat{\alpha} (-\nabla T)$, where $\hat{\sigma}$ and $\hat{\alpha}$ are the electrical and thermoelectric conductivity tensors, respectively. These transport coefficients can be calculated by Kubo formula once we obtain all the eigenstates of the Hamiltonian (in our calculation, σ_{xx} is obtained based on the calculation of the Thouless number²³). In practice, we can first calculate the $T = 0$ conductivities $\sigma_{ji}(E_F)$,

and then use the relation¹²

$$\begin{aligned}
\sigma_{ji}(E_F, T) &= \int d\epsilon \sigma_{ji}(\epsilon) \left(-\frac{\partial f(\epsilon)}{\partial \epsilon} \right), \\
\alpha_{ji}(E_F, T) &= \frac{-1}{eT} \int d\epsilon \sigma_{ji}(\epsilon) (\epsilon - E_F) \left(-\frac{\partial f(\epsilon)}{\partial \epsilon} \right), \tag{2}
\end{aligned}$$

to obtain the finite temperature electrical and thermoelectric conductivity tensors. Here, $f(x) = 1/[e^{(x-E_F)/k_B T} + 1]$ is the Fermi distribution function. At low temperatures, the second equation can be approximated as

$$\alpha_{ji}(E_F, T) = -\frac{\pi^2 k_B^2 T}{3e} \left. \frac{d\sigma_{ji}(\epsilon, T)}{d\epsilon} \right|_{\epsilon=E_F}, \tag{3}$$

which is the semiclassical Mott relation^{12,13}. The thermopower and Nernst signal can be calculated subsequently from³²

$$\begin{aligned}
S_{xx} &= \frac{E_x}{\nabla_x T} = \rho_{xx} \alpha_{xx} - \rho_{yx} \alpha_{yx}, \\
S_{xy} &= \frac{E_y}{\nabla_x T} = \rho_{xx} \alpha_{yx} + \rho_{yx} \alpha_{xx}. \tag{4}
\end{aligned}$$

The thermal conductivity, measuring the magnitude of the thermal currents in response to an applied temperature gradient, includes electron and phonon contributions. In our numerical calculations, phonon-derived thermal conductivity is omitted. The electronic thermal conductivities κ_{ji} at finite temperature assume the form¹³

$$\begin{aligned}
\kappa_{ji}(E_F, T) &= \frac{1}{e^2 T} \int d\epsilon \sigma_{ji}(\epsilon) (\epsilon - E_F)^2 \left(-\frac{\partial f(\epsilon)}{\partial \epsilon} \right) \\
&\quad - T \alpha_{ji}(E_F, T) \sigma_{ji}^{-1}(E_F, T) \alpha_{ji}(E_F, T). \tag{5}
\end{aligned}$$

For diffusive electronic transport in metals, it is well known that the Wiedemann-Franz law is satisfied between the electrical conductivity σ and the thermal conductivity κ of electrons³³:

$$\frac{\kappa}{\sigma T} = L, \tag{6}$$

where L is the Lorentz number and takes a constant value: $L = \frac{\pi^2}{3} \left(\frac{k_B}{e} \right)^2$.

III. THERMOELECTRIC TRANSPORT IN UNBIASED BILAYER GRAPHENE

We first show the calculated thermoelectric conductivities at finite temperatures for unbiased bilayer graphene. As seen from Fig.1(a) and (b), the transverse thermoelectric conductivity α_{xy} displays a series of peaks, while the longitudinal thermoelectric conductivity α_{xx} oscillates and changes sign at the center of each LL. At low temperatures, the peak of α_{xy} at the central LL is higher

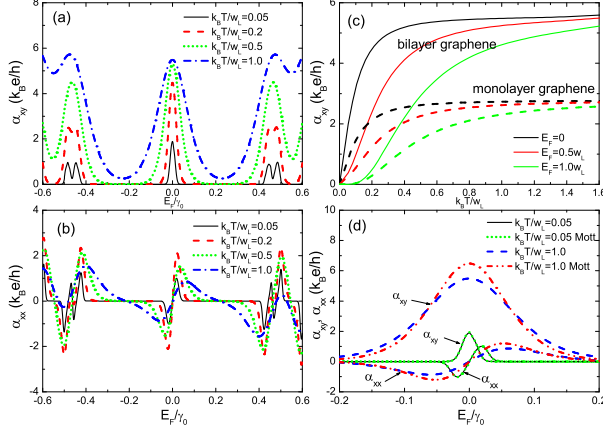


FIG. 1: (color online). Thermoelectric conductivities at finite temperatures of bilayer graphene. (a)-(b) $\alpha_{xy}(E_F, T)$ and $\alpha_{xx}(E_F, T)$ as functions of the Fermi energy at different temperatures. (c) shows the temperature dependence of $\alpha_{xy}(E_F, T)$ for monolayer and bilayer graphene. (d) compares the results from numerical calculations and from the generalized Mott relation at two characteristic temperatures, $k_B T/W_L = 0.05$ and $k_B T/W_L = 1$. The system size is taken to be $N = 96 \times 48 \times 2$, magnetic flux $\phi = 2\pi/48$, and disorder strength $r_s = 0.3$ (we consider uniformly distributed positive and negative charged impurities within this strength) with $W_L/\gamma_0 = 0.0376$.

and narrower than others, which indicates that the impurity scattering has less effect on the central LL. These results are qualitatively similar to those found in monolayer graphene⁹ due to the similar particle-hole symmetry in both cases, but some obvious differences exist. Firstly, the peak value of α_{xy} at the central LL is larger than that of monolayer graphene. Secondly, at low temperatures, α_{xy} splits around $E_F = \pm 0.46\gamma_0$, which can be understood as due to the presence of $\nu = \pm 8$ Hall plateau by lifting subband degeneracy. As shown in Fig.1(b), around the zero energy, the peak value of α_{xx} shows different trend with increasing temperature (it first increases with T at low-temperature region, and then it decreases with T at high temperatures). This is due to the competition between $\frac{\pi^2 k_B^2 T}{3e}$ and $\frac{d\sigma_{ji}(\epsilon, T)}{d\epsilon}$ of Eq.(3). The peak value of α_{xx} could either increase or decrease depending on the relative magnitudes of these two terms. At high temperatures, $\sigma_{ji}(\epsilon, T)$ becomes smooth, and consequently α_{xx} begins to decrease. In Fig.1(c), we find that α_{xy} shows different behavior depending on the relative strength of temperature $k_B T$ and the width of the central LL W_L (W_L is determined by the full-width at the half-maximum of the σ_{xx} peak). When $k_B T \ll W_L$ and $E_F \ll W_L$, α_{xy} shows linear temperature dependence, indicating that there is a small energy range where extended states dominate, and the transport falls into the semi-classical Drude-Zener regime. When E_F is shifted

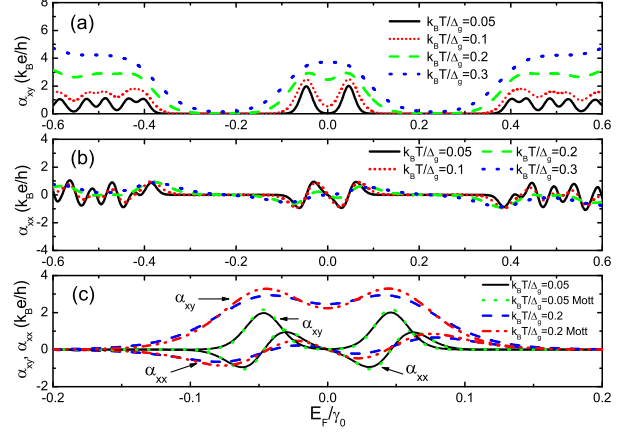


FIG. 2: (color online). Thermoelectric conductivities at finite temperatures of biased bilayer graphene. (a)-(b) $\alpha_{xy}(E_F, T)$ and $\alpha_{xx}(E_F, T)$ as functions of the Fermi energy at different temperatures. (c) Compares the results from numerical calculations and from the generalized Mott relation at two characteristic temperatures, $k_B T/\Delta_g = 0.05$ and $k_B T/\Delta_g = 0.2$. Here asymmetric gap $\Delta_g = 0.1\gamma_0$. The system size is taken to be $N = 96 \times 48 \times 2$, magnetic flux $\phi = 2\pi/48$, and disorder strength $r_s = 0.3$.

away from the Dirac point, the low-energy electron excitation is gapped due to Anderson localization. When $k_B T$ becomes comparable to or greater than W_L , the α_{xy} for all LLs saturates to a constant value $5.54k_B e/h$. This matches exactly the universal value $(\ln 2)k_B e/h$ predicted for the conventional IQHE systems in the case where thermal activation dominates^{12,13}, with an additional degeneracy factor 8. The saturated value of α_{xy} in bilayer graphene is exactly twice of that of monolayer graphene, as shown in Fig.1(c), in accordance with the eightfold degeneracy from valley, spin and layer degrees of freedom^{21,22}.

To examine the validity of the semiclassical Mott relation, we compare the above results with those calculated from Eq.(3), as shown in Fig.1(d). The Mott relation is a low-temperature approximation and predicts that the thermoelectric conductivities have linear temperature dependence. This is in agreement with our low-temperature results, which proves that the semiclassical Mott relation is asymptotically valid in Landau-quantized systems, as suggested in Ref. 12.

IV. THERMOELECTRIC TRANSPORT IN BIASED BILAYER GRAPHENE

For biased bilayer graphene, we show results of α_{xx} and α_{xy} at finite temperatures in Fig. 2. We see that α_{xy} displays a pronounced valley, in striking contrast to the unbiased case with a peak at the particle-hole sym-

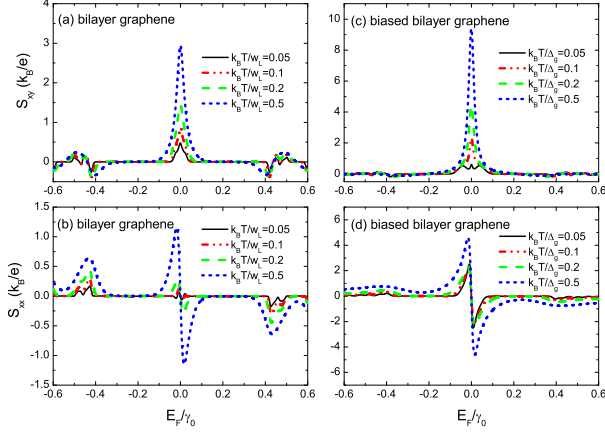


FIG. 3: (color online). The thermopower S_{xx} and the Nernst signal S_{xy} as functions of the Fermi energy in (a)-(b) bilayer graphene, (c)-(d) biased bilayer graphene at different temperatures. All parameters in this two systems are chosen to be the same as in Fig. 1 and Fig. 2, respectively.

metric point $E_F = 0$. This behavior can be understood as due to the split of the valley degeneracy in the central LL by an opposite voltage bias added to the two layers. This is in consistent with the opening of a sizable gap between the valence and conduction bands. More oscillations are observed in the higher LLs than the unbiased case, in consistent with the further lifting of the LL degeneracy in bilayer graphene. α_{xx} oscillates and changes sign around the center of each split LL. In Fig.2(c), we also compare the above results with those calculated from the semiclassical Mott relation using Eq.(3). The Mott relation is found to remain valid at low temperatures.

We further calculate the thermopower S_{xx} and the Nernst signal S_{xy} using Eq. (4), which can be directly determined in experiments by measuring the responsive electric fields. In Fig. 3(a)-(b), we show results of S_{xx} and S_{xy} in unbiased bilayer graphene. As we can see, S_{xy} (S_{xx}) has a peak at the central LL (the other LLs), and changes sign near the other LLs (the central LL), similar to the case of monolayer graphene⁹. This oscillatory feature has been observed experimentally³⁴. In our calculation, the peak value of S_{xx} at $n = -1$ LL is found to be $14\mu V/K$ (note that $k_B/e = 86.17\mu V/K$) for $k_B T = 0.05W_L$ and $26\mu V/K$ for $k_B T = 0.1W_L$, which is in agreement with the measured value $15\mu V/K$ ³⁴. At zero energy, both ρ_{xy} and α_{xx} vanish, leading to a vanishing S_{xx} . Around the zero energy, because $\rho_{xx}\alpha_{xx}$ and $\rho_{xy}\alpha_{xy}$ have opposite signs, depending on their relative magnitudes, S_{xx} could either increase or decrease when E_F is increased passing the Dirac point. In bilayer graphene, we find that S_{xx} is always dominated by $\rho_{xy}\alpha_{xy}$, and consequently S_{xx} decreases to negative value as E_F passing the Dirac point. We find that the peak value of S_{xx} in the central LL is $\pm 6\mu V/K$ at

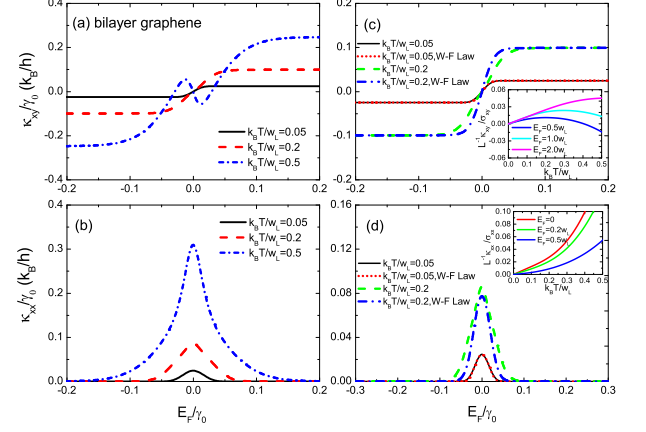


FIG. 4: (color online). (a)-(b) Thermal conductivities $\kappa_{xy}(E_F, T)$ and $\kappa_{xx}(E_F, T)$ as functions of the Fermi energy in bilayer graphene at different temperatures, (c)-(d) Compares the thermal conductivity as functions of the Fermi energy from numerical calculations and from the Wiedemann-Franz law at two characteristic temperatures. The parameters chosen here are the same as in Fig. 1.

$k_B T = 0.05W_L$. On the other hand, S_{xy} has a peak structure at zero energy, which is dominated by $\rho_{xx}\alpha_{xy}$. The peak value is $42\mu V/K$ at $k_B T = 0.05W_L$, which is in good agreement with the experimental value $40\mu V/K$ ³⁴.

In Fig. 3(c)-(d), we show the calculated S_{xx} and S_{xy} in biased bilayer graphene system. As we can see, S_{xy} (S_{xx}) has a peak around zero energy (the other LLs), and changes sign near the other LLs (zero energy). In our calculation, S_{xx} is dominated by $\rho_{xx}\alpha_{xx}$, which is different from unbiased bilayer graphene. At low temperatures, the peak value of S_{xx} near zero energy keeps almost unchanged around $\pm 181\mu V/K$, which is much larger than that of unbiased case. With the increase of temperature, the peak height increases to $\pm 396\mu V/K$ at $k_B T = 0.5\Delta_g$. Theoretical study²⁰ indicates that, the large magnitude of S_{xx} is mainly a result of the energy gap. On the other hand, S_{xy} has a peak structure around zero energy, which is dominated by $\alpha_{xy}\rho_{xx}$. With $\sigma_{xx} \sim 2e^2/h$ near $E_F = 0$, we find that the peak height is $198\mu V/K$ at $k_B T = 0.1\Delta_g$, which is larger than that of unbiased case.

V. THERMAL CONDUCTIVITY FOR UNBIASED AND BIASED BILAYER GRAPHENE SYSTEMS

We now focus on thermal conductivities. In Fig. 4, we plot results of the transverse thermal conductivity κ_{xy} and the longitudinal thermal conductivity κ_{xx} for unbiased bilayer graphene at different temperatures. As seen from Fig.4(a) and (b), κ_{xy} exhibits two flat plateaus

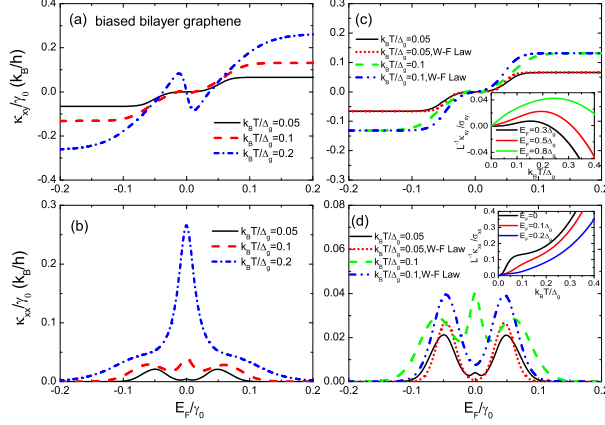


FIG. 5: (color online). (a)-(b) Thermal conductivities $\kappa_{xy}(E_F, T)$ and $\kappa_{xx}(E_F, T)$ as functions of the Fermi energy in biased bilayer graphene at different temperatures, (c)-(d) Compares the thermal conductivity as functions of the Fermi energy from numerical calculations and from the Wiedemann-Franz law at two characteristic temperatures. The parameters chosen here are the same as in Fig. 2.

away from the center of the central LL. At low temperatures, the transition between these two plateaus is smooth and monotonic, while at higher temperatures, κ_{xy} exhibits an oscillatory feature at $k_B T = 0.5W_L$ between two plateaus. On the other hand, κ_{xx} displays a peak near the center of the central LL, while its peak value increases quickly with T . To test the validity of the Wiedemann-Franz law, we compare the above results with those calculated from Eq.(6) as shown in Fig.4(c) and (d). The Wiedemann-Franz law predicts that the ratio of the thermal conductivity κ to the electrical conductivity σ of a metal is proportional to the temperature. This is in agreement with our low-temperature results, while deviation is seen at relatively high temperatures.

In Fig. 5, we show the calculated thermal conductivities κ_{xx} and κ_{xy} for biased bilayer graphene. As seen from Fig.5(a) and (b), around zero energy, a flat region with $\kappa_{xy} = 0$ is found at low temperatures, which is accompanied by a valley in κ_{xx} . These features are clearly in contrast to those of unbiased case due to the asymmetric gap between the valence and conduction bands. When temperature increases to $k_B T = 0.2\Delta_g$, the plateau of $\kappa_{xy} = 0$ disappears, while κ_{xx} displays a large peak. In Fig.5(c) and (d), we also compare the above results with those calculated from the Wiedemann-Franz law using Eq.(6). Due to the presence of energy gap, we find that the Wiedemann-Franz law is not valid in biased bilayer graphene.

VI. SUMMARY

In summary, we have numerically investigated the thermoelectric and thermal transport in unbiased bilayer graphene based on the tight-binding model in the presence of both disorder and magnetic field. We find that the thermoelectric conductivities display different asymptotic behaviors depending on the ratio between the temperature and the width of the disorder-broadened Landau levels (LLs), similar to those found in monolayer graphene. In the high temperature regime, the transverse thermoelectric conductivity α_{xy} saturates to a universal value $5.54k_B e/h$ at the center of each LL, and displays a linear temperature dependence at low temperatures. The calculated Nernst signal S_{xy} shows a peak at the central LL with heights of the order of k_B/e , and changes sign at the other LLs, while the thermopower S_{xx} has an opposite behavior. These results are in good agreement with the experimental observation³⁴. The validity of the semiclassical Mott relation between the thermoelectric and electrical transport coefficients is verified in a range of temperatures. The calculated transverse thermal conductivity κ_{xy} exhibits two plateaus away from the band center. The transition between these two plateaus is continuous, which is accompanied by a pronounced peak in longitudinal thermal conductivity κ_{xx} . The validity of the Wiedemann-Franz law relating the thermal conductivity κ and the electrical conductivity σ is verified to be satisfied only at very low temperatures.

We further discuss the thermoelectric transport of biased bilayer graphene. When a bias is applied to the two graphene layers, the thermoelectric coefficients exhibit unique characteristics different from those of unbiased case. Around the Dirac point, transverse thermoelectric conductivity exhibits a pronounced valley with $\alpha_{xy} = 0$ at low temperatures, and the thermopower displays a strong peak. Furthermore, the transverse thermal conductivity has a pronounced plateau with $\kappa_{xy} = 0$, which is accompanied by a valley in κ_{xx} . These are consistent with the opening of sizable gap between the valence and conductance bands in biased bilayer graphene.

We mention that in our numerical calculations, the flux $2\pi/M$ in each hexagon gives a magnetic field of the strength $B \sim 1.3 \times 10^5/M$ Tesla³⁵. Thus the magnetic field B we used is about 2700 Tesla. This magnetic field is much stronger than the ones which can be realized in the experimental situation, as limited by current computational capability. In our calculation, the system size is taken to be $N = 96 \times 48 \times 2$, and M is taken to be L_x or L_y , in order to use periodic boundary conditions, which limits us to extremely strong magnetic field. However, the obtained thermoelectric transport coefficients exhibit universal behaviors, as long as M is not too small (of the order 10 or greater).

Acknowledgments

This work is supported by the DOE Office of Basic Energy Sciences under grant DE-FG02-06ER46305 (RM, DNS), and the U.S. DOE through the LDRD program at LANL (LZ), the NSF Grant DMR-0906816 (RM), and the Scientific Research Foundation of Nanjing University of Information and Technology of China under Grant No. 20100401 (RM). We also thank partial

support from Princeton MRSEC Grant DMR-0819860, the NSF instrument grant DMR-0958596 (DNS), the NSFC Grant No. 10874066, the National Basic Research Program of China under Grant Nos. 2007CB925104 and 2009CB929504 (LS), and the doctoral foundation of Chinese Universities under Grant No. 20060286044 (ML).

-
- ¹ Y.M. Zuev, W. Chang, and P. Kim, Phys. Rev. Lett. **102**, 096807 (2009).
 - ² P. Wei, W. Bao, Y. Pu, C. N. Lau, and J. Shi, Phys. Rev. Lett. **102**, 166808 (2009).
 - ³ J.G. Checkelsky and N.P. Ong, Phys. Rev. B **80**, 081413(R) (2009).
 - ⁴ A. H. Castro Neto, F. Guinea, N. M. R. Peres, K. S. Novoselov and A. K. Geim, Rev. Mod. Phys. **81**, 109 (2009).
 - ⁵ E. H. Hwang, E. Rossi, and S. Das Sarma, Phys. Rev. B **80**, 235415 (2009).
 - ⁶ T. Löfwander and M. Fögelstrom, Phys. Rev. B **76**, 193401 (2007).
 - ⁷ B. Dóra and P. Thalmeier, Phys. Rev. B **76**, 035402 (2007).
 - ⁸ X.-Z. Yan, Y. Romiah, and C. S. Ting, Phys. Rev. B **80**, 165423 (2009).
 - ⁹ L. Zhu, R. Ma, L. Sheng, M. Liu, and D. N. Sheng, Phys. Rev. Lett. **104**, 076804 (2010).
 - ¹⁰ S. M. Girvin and M. Jonson, J. Phys. C **15**, L1147(1982).
 - ¹¹ P. Středa, J. Phys. C **16**, L369 (1983).
 - ¹² M. Jonson and S.M. Girvin, Phys. Rev. B **29**, 1939 (1984).
 - ¹³ H. Oji, J. Phys. C **17**, 3059 (1984).
 - ¹⁴ E. McCann, Phys. Rev. B **74**, 161403(R) (2006).
 - ¹⁵ H. Min, B. Sahu, S. K. Banerjee, and A. H. MacDonald, Phys. Rev. B **75**, 155115 (2007).
 - ¹⁶ E. V. Castro, K. S. Novoselov, S. V. Morozov, N. M. R. Peres, J. M. B. Lopes dos Santos, J. Nilsson, F. Guinea, A. K. Geim, and A. H. Castro Neto, Phys. Rev. Lett. **99**, 216802 (2007).
 - ¹⁷ J. B. Oostinga, H. B. Heersche, X. Liu, A. F. Morpurgo, and L. M. K. Vandersypen, Nat. Mater. **7**, 151 (2008).
 - ¹⁸ Y. Zhang, T.-T. Tang, C. Girit, Z. Hao, M. C. Martin, A. Zettl, M. F. Crommie, Y. R. Shen, and F. Wang, Nature **459**, 820 (2009).
 - ¹⁹ K. F. Mak, C. H. Lui, J. Shan, and T. F. Heinz, Phys. Rev. Lett. **102**, 256405 (2009).
 - ²⁰ L. Hao and T. K. Lee, Phys. Rev. B **81**, 165445 (2010).
 - ²¹ E. McCann and V. I. Falko, Phys. Rev. Lett. **96**, 086805 (2006).
 - ²² K. S. Novoselov, E. McCann, S. V. Morozov, V. I. Fal'ko, M. I. Katsnelson, U. Zeitler, D. Jiang, F. Schedin and A. K. Geim, Nature Phys. **2**, 177 (2006).
 - ²³ R. Ma, L. Sheng, R. Shen, M. Liu and D. N. Sheng, Phys. Rev. B **80**, 205101 (2009); R. Ma, L. Zhu, L. Sheng, M. Liu, D. N. Sheng, Europhys. Lett. **87**, 17009 (2009).
 - ²⁴ S. B. Trickey, F. Muller-Plathe, G. H. F. Dierksen and J. C. Boettger, Phys. Rev. B **45**, 4460 (1992).
 - ²⁵ K. Yoshizawa, T. Kato, and T. Yamabe, J. Chem. Phys. **105**, 2099 (1996); T. Yumura and K. Yoshizawa, Chem. Phys. **279**, 111 (2002).
 - ²⁶ D.N. Sheng, L. Sheng, and Z.Y. Weng, Phys. Rev. B **73**, 233406 (2006).
 - ²⁷ S. Das Sarma, S. Adam, E. H. Hwang and E. Rossi, Rev. Mod. Phys. **83**, 407 (2011).
 - ²⁸ S. Adam and S. Das Sarma, Solid State Communications **146**, 356 (2008).
 - ²⁹ Y. W. Tan, Y. Zhang, K. Bolotin, Y. Zhao, S. Adam, E. H. Hwang, S. Das Sarma, H. L. Stormer, and P. Kim, Phys. Rev. Lett. **99**, 246803 (2007).
 - ³⁰ J. H. Chen, C. Jang, S. Adam, M. S. Fuhrer, E. D. Williams, and M. Ishigami, Nature Physics **4**, 377 (2008).
 - ³¹ S. Adam, E. H. Hwang, V. M. Galitski, and S. Das Sarma, Proc. Natl. Acad. Sci. USA **104**, 18392 (2007).
 - ³² Different literatures may have a sign difference due to different conventions.
 - ³³ J. M. Ziman, Electrons and Phonons: The Theory of Transport Phenomena in Solids (Oxford University Press, Oxford, 1963).
 - ³⁴ S.G. Nam, D.K. Ki, H.J. Lee, Phys. Rev. B **82**, 245416 (2010).
 - ³⁵ B. A. Bernevig, T. L. Hughes, H. Chen, C. Wu, and S. C. Zhang, Int. J. Mod. Phys. B **20**, 3257 (2006).